Effects of atmospheric sphericity on stratospheric chemistry and dynamics over Antarctica

Jun-ichi Kurokawa,[1] Hideharu Akiyoshi,[2] Tatsuya Nagashima,[2] Hirohiko Masunaga,[3] Teruyuki Nakajima,[4] Masaaki Takahashi,[4] and Hideaki Nakane[2]

Received 25 January 2005; revised 18 July 2005; accepted 8 August 2005; published 4 November 2005.

[1] Atmospheric sphericity is an important factor that must be considered in order to evaluate an accurate ozone loss rate in the polar stratosphere. The built-in plane-parallel radiative transfer scheme of a nudging chemical transport model (CTM) and an atmospheric general circulation model (AGCM) with coupled chemistry is modified by a pseudospherical approximation. The plane-parallel atmosphere radiative transfer version (PPA version) is compared with the pseudospherical atmosphere radiative transfer version (SA version) for both the nudging CTM and AGCM. The nudging CTM can isolate the chemical effects for a given dynamical field, while the interaction among the chemical, radiative, and dynamical processes can be studied with the AGCM. The present analysis focuses on Antarctica during an ozone hole period. In the ozone loss period over Antarctica, ozone starts to decrease earlier and minimum value of total ozone becomes lower in the SA versions of both the nudging CTM and the AGCM than in the corresponding PPA versions. The ozone mixing ratio decreases earlier in the SA version because of an earlier increase of ClO concentration initiated by the upward actinic flux at solar zenith angles greater than 90°. Dynamics plays an important role as well as the chemical processes. During the ozone recovery period, the ozone distribution becomes almost the same in the SA and PPA versions of the nudging CTM, while in the AGCM the ozone amount in the SA version remains at lower values compared to those of the PPA version. In the AGCM, a decrease of ozone over Antarctica enhances the latitudinal gradient of temperature and thus strengthens the polar vortex in the SA version. A resultant delay of the polar vortex breakup causes the delay of the ozone recovery. For the AGCM, ensemble runs are performed. The ensemble experiment exhibits large ozone variances after the middle of December, when the ozone recovery is dynamically controlled. Most ensemble members of the AGCM show a delay of the polar vortex breakup in the SA version, while a few members show opposite results. In the latter members, the polar vortex breakup is strongly affected by the enhanced EP flux from the troposphere around 100 hPa, which causes the variances in the ozone recovery period. Most members, however, do not show large statistical variances; that justifies the conclusions from the ensemble means.

Citation: Kurokawa, J., H. Akiyoshi, T. Nagashima, H. Masunaga, T. Nakajima, M. Takahashi, and H. Nakane (2005), Effects of atmospheric sphericity on stratospheric chemistry and dynamics over Antarctica, *J. Geophys. Res.*, *110*, D21305, doi:10.1029/2005JD005798.

1. Introduction

[2] In order to evaluate an accurate ozone loss rate in the polar stratosphere, atmospheric sphericity is an important factor that must be considered because the ozone hole starts at the end of the polar night, when solar zenith angles (SZAs) are greater than 90°. The effects of atmospheric sphericity have been studied using multidimensional models with radiative transfer schemes for a spherical atmosphere or with a pseudospherical approximation. The performance of such schemes has been justified by many previous studies [*Lary and Pyle*, 1991a, 1991b; *Lary et al.*, 1991; *Perner et al.*, 1991; *Dahlback and Stamnes*, 1991; *Dvortsov et al.*, 1992; *Müller et al.*, 1994; *Rattigan et al.*, 1996; *Chipperfield et al.*, 1998; *Kylling et al.*, 2003].

[3] Recently, the effects of atmospheric sphericity on the dynamics and chemistry of the global lower stratosphere have been studied by *Lamago et al.* [2003] with a coupled chemistry-climate model. They performed calculations with

[1]Fujitsu FIP Corporation, Tokyo, Japan.
[2]National Institute for Environmental Studies, Tsukuba, Japan.
[3]Department of Atmospheric Science, Colorado State University, Fort Collins, Colorado, USA.
[4]Center for Climate System Research, University of Tokyo, Tokyo, Japan.

0148-0227/05/2005JD005798$09.00

and without photolysis for SZAs between 87.5° and 93°. Photolysis rates for SZAs less equal than 87.5° were calculated using the method of *Landgraf and Crutzen* [1998], while those for larger SZAs were computed using an empirical formula, where the photolysis rates were multiplied by a correction factor [*Levy*, 1974; *Röth*, 1992, 2002]. They showed that in the polar Southern Hemisphere, total ozone was reduced by about 20% in the simulation with photolysis for SZAs between 87.5° and 93° because ozone destruction started earlier (at larger SZAs), and therefore the loss period became longer. They also showed that a cooling of the polar lower stratosphere (at 50 hPa) of up to −4K was caused by a chemical-radiative-dynamical coupling response to the solar flux at large SZAs.

[4] We have developed (1) a three-dimensional stratospheric model with fully interactive chemistry based on the Center for Climate System Research (CCSR)/National Institute for Environmental Studies (NIES) Atmospheric General Circulation Model (AGCM) [*Numaguti*, 1993; *Numaguti et al.*, 1995, 1997; *Takigawa et al.*, 1999; *Nagashima et al.*, 2002] and (2) a nudged version of the model (hereafter, a nudging chemical transport model (CTM)) that assimilates the observed wind and temperature fields into the CCSR/NIES AGCM using nudging methods [*Akiyoshi et al.*, 2002a, 2002b, 2004]. In these models, photolysis rates are calculated using the actinic flux from a plane-parallel radiative transfer scheme. The actinic flux in the plane-parallel scheme is accurate enough when SZAs are small, but the error becomes larger as SZAs approach 90°. Furthermore, the plane-parallel scheme does not treat actinic flux at SZAs larger than 90°.

[5] In this paper, the effects of the sphericity of the atmosphere are incorporated by modifying the plane-parallel scheme with a pseudospherical approximation for radiative transfer calculations. This modified scheme is introduced to both the nudging CTM and the AGCM with coupled chemistry. In the nudging CTM, the dynamical fields are specified by observations and therefore the chemical effects of the atmospheric sphericity for a given dynamical field can be isolated. In the AGCM with coupled chemistry, on the other hand, ozone changes affect the temperature and circulation interactively and therefore the effects of atmospheric sphericity on the interactions among the chemical, radiative, and dynamical processes can be studied. The present analysis focuses on Antarctica during an ozone hole period.

[6] Section 2 briefly describes the procedure for extension of the plane-parallel radiative transfer scheme for large SZAs. The models and the layouts of the experiments are described in section 3. The results of the nudging CTM and the AGCM with coupled chemistry are analyzed in section 4 and discussions are presented in section 5. Finally, section 6 gives the conclusions of this paper.

2. Extension of the Plane-Parallel Radiative Transfer Scheme for Photolysis Rate Calculations at Large SZAs

[7] The nudging CTM and the AGCM with coupled chemistry calculate photolysis rates using the actinic flux calculated in the radiative transfer scheme of the models. The original radiative transfer scheme of the models is a two-stream discrete ordinates method assuming a plane-parallel atmosphere [*Nakajima and Tanaka*, 1986; *Nakajima et al.*, 2000; *Numaguti*, 1993; *Numaguti et al.*, 1995, 1997]. The computation of the fluxes involved in the photolysis rate calculations is done in six spectral bins (200.0–217.4, 217.4–232.6, 277.8–289.9, 289.9–303.0, 303.0–317.5, and 317.5–689.7 nm). The concentrations of chemical species calculated in the models are used in the radiative transfer scheme. The background aerosol concentration in the troposphere is assumed to be 1.0×10^{-12} cm^3/cm^3 and is assumed to be zero in the stratosphere.

[8] In the models, photolysis rates are calculated as follows [*Akiyoshi*, 1997]:

$$J_i(Z) = \sum\nolimits_{\lambda} j_i(Z, \lambda)$$

$$j_i(Z, \lambda) = \left(\overline{I^-(Z, \lambda)} + \overline{I^+(Z, \lambda)}\right) \times \sigma_i(\lambda, T(Z)) \times q_i(\lambda) \times \frac{\lambda}{hc},$$

where $J_i(Z)$ is the spectrally integrated photolysis rate of chemical species i at altitude Z, $j_i(Z, \lambda)$ is that in spectral bin λ, $\overline{I^{\mp}(Z, \lambda)}$ represents the downward (−) and upward (+) actinic flux at altitude Z in spectral bin λ, $\sigma_i(\lambda, T(Z))$ is the absorption cross section of species i at temperature $T(Z)$ at Z in spectral bin λ, $q_i(\lambda)$ is the quantum yield of species i in spectral bin λ, h is Planck's constant, and c is the velocity of light. Note that the interval of the last spectral bin (317.5–689.7 nm) is too large to calculate accurate photolysis rates. In this spectral bin, photolysis rates are calculated using weighted mean cross sections of chemical species. The weighted mean absorption cross sections were calculated using the monochromatic solar flux at the top of the atmosphere as weighting factors [*Akiyoshi*, 1997]. Wavelengths of less than 200 nm are not considered in the radiative transfer schemes of the models. Thus the photolysis rates in the Schumann-Runge band are calculated with the parameterization developed by *Minschwaner et al.* [1993] and *Allen and Frederick* [1982].

[9] The nudging CTM and the AGCM with coupled chemistry with the plane-parallel scheme have reproduced realistic seasonal and day-to-day variations and global distributions of chemical compounds in the stratosphere [*Takigawa et al.*, 1999; *Akiyoshi et al.*, 2002a, 2002b, 2004; *Nagashima et al.*, 2002]. However, the optical path of direct solar incidence in the plane-parallel scheme is overestimated everywhere, especially when SZAs are close to 90°, which results in the underestimation of photolysis rates. Moreover, plane-parallel approximation cannot treat the solar direct radiation at SZAs greater than 90°.

[10] In order to overcome these deficiencies, the plane-parallel radiative transfer scheme is modified using a pseudospherical approximation as follows: (1) The upward solar direct radiation at SZAs greater than 90° is added. (2) The single-scattering phase function for the upward solar direct radiation is added. (3) The Chapman function is modified to consider the atmospheric sphericity with the method of *Dahlback and Stamnes* [1991] and is used for both the downward and upward solar direct radiation. Then, downward and upward actinic fluxes at vertical

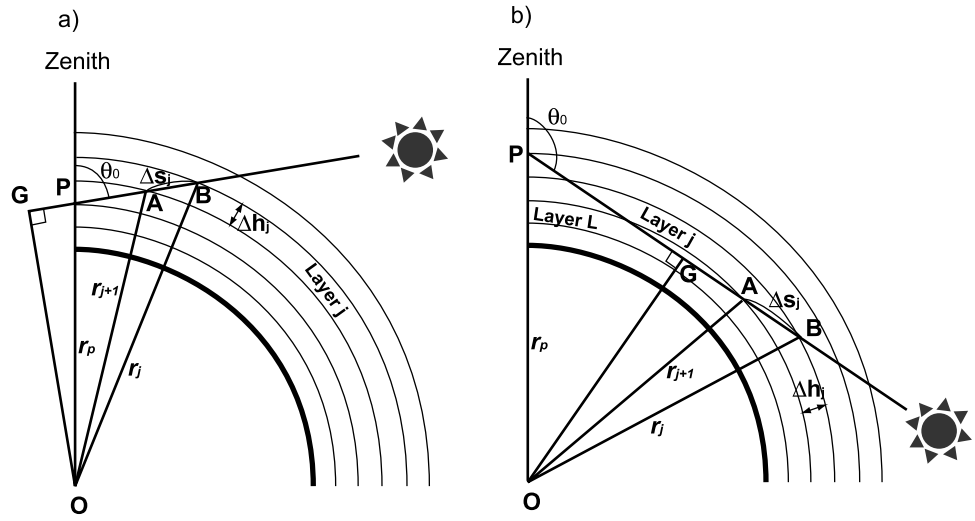

Figure 1. Geometry of direct sunlight used to calculate the Chapman function in a spherically layered atmosphere. (a) SZAs $\theta_0 < 90°$ and (b) SZAs $\theta_0 \geq 90°$.

optical depths $\tau = \tau(Z)$ in spectral bin λ are obtained depending on the value of SZA, θ_0, as follows:

For $\theta_0 < 90°$

$$\overline{I^-(\tau,\lambda)} = F^-_{diffuse} + I_0 e^{-ch(\tau,\theta_0)}$$

$$\overline{I^+(\tau,\lambda)} = F^+_{diffuse}$$

For $\theta_0 \geq 90°$

$$\overline{I^-(\tau,\lambda)} = F^-_{diffuse}$$

$$\overline{I^+(\tau,\lambda)} = F^+_{diffuse} + I_0 e^{-ch(\tau,\theta_0)},$$

where $F^{\mp}_{diffuse}$ is the diffuse component of the downward (−) and the upward (+) solar flux, $I_0 e^{-ch(\tau,\theta_0)}$ is the direct component of the solar flux, and $ch(\tau, \theta_0)$ is the Chapman function, which represents the optical path of direct solar incidence through a spherical atmosphere. The Chapman function is given as follows using the formulation of *Dahlback and Stamnes* [1991]:

For $\theta_0 < 90°$

$$ch(\tau,\theta_0) = \sum_{j=1}^{p} \Delta\tau_j \left(\frac{\Delta s_j}{\Delta h_j}\right)$$

For $\theta_0 \geq 90°$

$$ch(\tau,\theta_0) = \sum_{j=1}^{p} \Delta\tau_j \left(\frac{\Delta s_j}{\Delta h_j}\right) + 2\sum_{j=p+1}^{L-1} \Delta\tau_j \left(\frac{\Delta s_j}{\Delta h_j}\right) + \Delta\tau_L \left(\frac{\Delta s_L}{\Delta h_L}\right)$$

where $\Delta\tau_j$ is the plane-parallel optical depth of each layer j, $\Delta h_j = r_j - r_{j+1}$, and $\Delta s_j = AB = GB - GA = \sqrt{OB^2 - OG^2} - \sqrt{OA^2 - OG^2} = \sqrt{r_j^2 - r_p^2 \sin^2\theta_0} - \sqrt{r_{j+1}^2 - r_p^2 \sin^2\theta_0}$ (see Figure 1). L is the deepest layer in the atmosphere where the attenuation of the direct beam must be considered.

[11] The diurnally averaged photolysis rates of Cl_2O_2 at the winter solstice by the new scheme are shown in

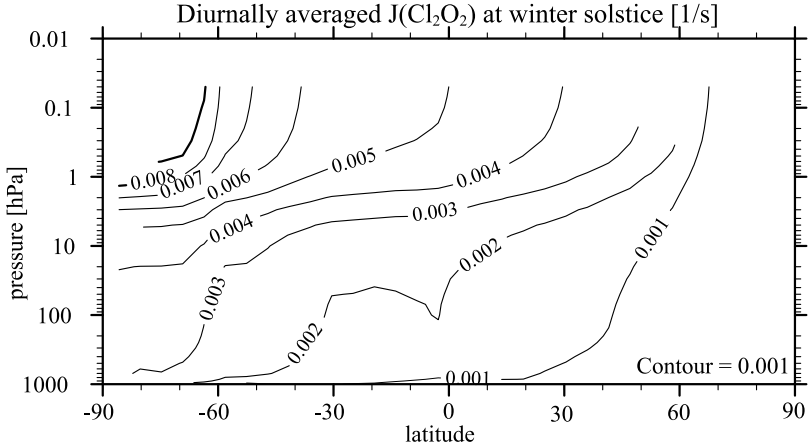

Figure 2. A latitude-height cross section of the diurnally averaged photolysis rates of Cl_2O_2 at the winter solstice calculated with the new pseudospherical scheme.

Table 1. Photolysis Rates of Cl_2O_2, HOCl, HOBr, and H_2O_2 at Local Noon at 80°S, 50 hPa, and Solar Zenith Angles (SZAs) From 70° to 94.23°, Calculated by the Spherical Radiative Transfer Version

	Photolysis Rates for Each SZA Greater Than 70°								
	70°	80°	85°	88°	89°	90°	91°	92°	93°	94.23°
$J(Cl_2O_2)$[a]	3.400×10^{-3}	2.660×10^{-3}	2.144×10^{-3}	1.691×10^{-3}	1.531×10^{-3}	1.052×10^{-3}	2.083×10^{-4}	7.576×10^{-5}	$1.019 \times x10^{-5}$	1.416×10^{-7}
J(HOCl)[b]	4.517×10^{-4}	3.533×10^{-4}	2.848×10^{-4}	2.248×10^{-4}	2.030×10^{-4}	1.398×10^{-4}	2.769×10^{-5}	1.007×10^{-5}	1.355×10^{-6}	1.880×10^{-8}
J(HOBr)[c]	4.678×10^{-3}	3.661×10^{-3}	3.072×10^{-3}	2.457×10^{-3}	2.226×10^{-3}	1.532×10^{-3}	3.027×10^{-4}	1.099×10^{-4}	1.464×10^{-5}	1.937×10^{-7}
$J(H_2O_2)$[d]	9.799×10^{-6}	7.510×10^{-6}	5.475×10^{-6}	4.152×10^{-6}	3.746×10^{-6}	2.574×10^{-6}	5.115×10^{-7}	1.865×10^{-7}	2.585×10^{-8}	4.037×10^{-10}

[a] $J(Cl_2O_2)$:$Cl_2O_2 + h\nu \rightarrow ClOO + Cl$, sec^{-1}.
[b] $J(HOCl)$:$HOCl + h\nu \rightarrow OH + Cl$, sec^{-1}.
[c] $J(HOBr)$:$HOBr + h\nu \rightarrow OH + Br$, sec^{-1}.
[d] $J(H_2O_2)$:$H_2O_2 + h\nu \rightarrow 2OH$, sec^{-1}.

Figure 2. The results generally agree with those of *Lary and Pyle* [1991a]. The photolysis rates of Cl_2O_2, HOCl, HOBr, and H_2O_2 at local noon at 80°S, 50 hPa, and SZAs from 70° to 94.23° are also presented in Table 1. The maximum SZA is 94.23° at 80°S and 50 hPa. In the new scheme, the solar direct radiation at SZAs greater than 90° is considered except where the model grid is in the shadow of the earth. Therefore the maximum SZA for a given grid box in this scheme depends on its latitude and altitude.

3. Model Description and Numerical Experiments

[12] In this work, we use two types of three-dimensional stratospheric chemical models. One is a nudging CTM and the other is an AGCM with coupled chemistry. The chemical scheme for the nudging CTM includes gas phase chemical reactions of O_x, HO_x, NO_x, hydrocarbons, ClO_x, and BrO_x, and heterogeneous reactions on nitric acid trihydrate (NAT), water ice, and supercooled ternary solution (STS) polar stratospheric clouds [*Akiyoshi et al.*, 2004]. On the other hand, the scheme for the AGCM is slightly simplified to circumvent the large computation time required for the ensemble experiment. In particular, it does not include bromine chemistry or heterogeneous reactions on STS [see *Takigawa et al.*, 1999; *Nagashima et al.*, 2002]. However, the strength of ozone destruction by bromine species is much smaller than that by chlorine species over Antarctica and the time evolution of ozone destruction rate due to bromine species is similar to that due to chlorine species, especially in the ozone loss phase (see Figure 13). Therefore omitting these aspects of chemistry in the AGCM does not reduce the validity of the results and conclusions of this paper. Both models have 34 vertical atmospheric layers that extend from the surface to about 80 km with a horizontal resolution T21 (longitude × latitude ≈ 5.6° × 5.6°).

[13] In the nudging CTM, observed wind and temperature fields are assimilated into the AGCM by adding the nudging terms to the time tendency equations for zonal wind velocity, meridional wind velocity, and temperature,

$$-(x - x_{obs})/\tau, \quad x = \mathrm{u}, \mathrm{v}, \text{ and } \mathrm{T},$$

where u is the zonal wind velocity; v is the meridional wind velocity; T is the temperature; x are the model calculated values of u, v, and T; x_{obs} are the observed values of u, v, and T; and τ is the timescale of the nudging. Then, the u, v, and T values in the nudging CTM tend to approach observed values with a timescale of τ. A timescale of one day is used for this study. Below 10 hPa, the European Centre for Medium-Range Weather Forecast (ECMWF) analysis data are used. Above 10 hPa, where no ECMWF data exist, the monthly and zonal mean zonal wind and temperature data of the Committee on Space Research (COSPAR) International Reference Atmosphere 86 (CIRA1986) [*Rees et al.*, 1990] are used. The meridional wind above 10 hPa is not nudged but is calculated by the continuity equation in the model (see *Akiyoshi et al.* [2004] for details).

[14] We perform the integration of the nudging CTM and the AGCM with coupled chemistry both with the plane-parallel and the pseudospherical radiative transfer schemes. The runs of the nudging CTM are performed from 1 January to 31 December 1999 using the same initial and surface

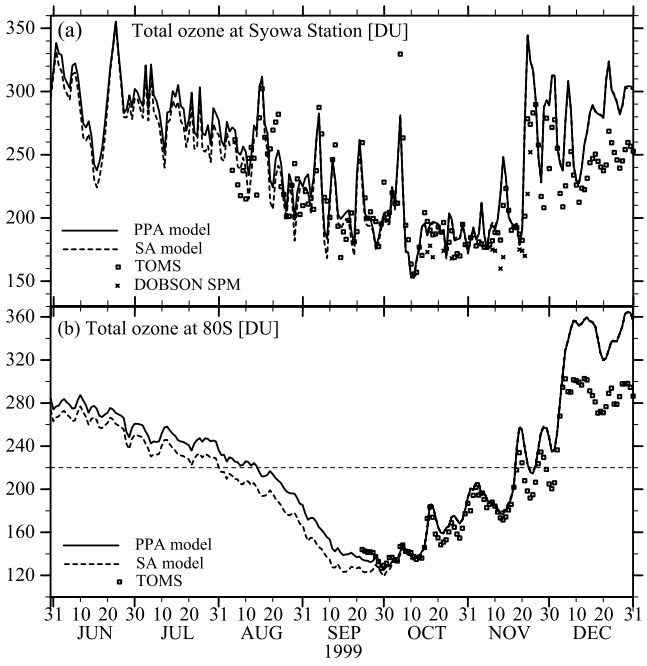

Figure 3. Time evolution of (a) the total ozone at Syowa Station and (b) the zonal mean total ozone over 80°S simulated by the nudging CTM and observed by TOMS and the Dobson spectrophotometer (DOBSON SPM) at the station from June to December 1999. Solid and dashed lines indicate the calculated results from the PPA and SA versions, respectively; the open squares denote the TOMS observations; and the diagonal crosses denote the Dobson spectrophotometer observations. The horizontal dashed line indicates the ozone hole criterion of <220 D.U.

boundary conditions. The initial conditions are prepared by a spin-up run by the nudging CTM with the plane-parallel scheme under conditions typical of the 1990s. The boundary conditions are obtained from *World Meteorological Organization* (*WMO*) [1999] surface concentration of CFCs and greenhouse gases. For the AGCM with coupled chemistry, the 24 different initial conditions for 1 January are prepared from the outputs of spin-up runs under conditions typical of the 1990s using the AGCM with the plane-parallel scheme. Then ensemble runs are performed for a 14-month period from 1 January to the end of February of the following year. The surface boundary conditions for the AGCM are also specified by *WMO* [1999].

4. Results

4.1. Effects of Atmospheric Sphericity on Polar Chemistry: Results From the Nudging CTM Simulation

[15] A comparison of the simulated and observed time evolution of total ozone during the Southern Hemisphere ozone hole period of 1999 is shown in Figure 3. Figure 3a shows the time evolution of the total ozone at Syowa Station (69°S 39.5°E) calculated with the plane-parallel atmosphere version (hereafter, the PPA version) and the pseudospherical atmosphere version (hereafter, the SA version) of the radiative transfer schemes. Observations by the Total Ozone Mapping Spectrometer (TOMS) and the Dobson spectrophotometer at the station are also shown. The zonal mean total ozone at the slightly higher latitude of 80°S is also compared with TOMS in Figure 3b. The nudging CTM successfully simulates the variation and minimum value of the total ozone during the ozone loss phase as well as during the ozone recovery phase. In this and the next subsection, the effects of atmospheric sphericity on the chemistry and dynamics are studied in detail at 80°S. This latitude is located sufficiently far from the model boundary of both the polar vortex and the South Pole.

[16] The difference in the time evolution of the zonal mean total ozone between the SA and PPA versions is seen in Figure 3b. In the SA version, onset of the ozone hole (defined as the region of total ozone values less than 220 D.U.) in August shifts to earlier dates, and the minimum value of total ozone becomes lower in comparison with the PPA version. On the other hand the variation and the absolute value in the recovery phase are almost the same between the two models versions. A similar feature is also seen in Figure 3a. These behaviors are clearly shown in Figure 4, where the difference in the zonal mean total ozone between the SA and PPA versions (SA minus PPA) at 80°S is plotted. The difference starts to increase at the beginning of July, continues to increase until the end of August, and then diminishes rapidly by the end of September.

[17] In order to understand these features of the total ozone during the ozone hole period, the temporal evolution of the ozone mixing ratio simulated by the SA and PPA versions at 80°S and 50 hPa from 1 June to 31 December 1999, and the difference between the SA version and the PPA versions (SA minus PPA) are shown in Figures 5a and 5b. The ozone amount at 50 hPa contributes largely to the total ozone, and the difference between the SA and PPA versions is evident at this altitude. Figures 5c and 5d show the ClO mixing ratio, and the photolysis rates of Cl_2O_2. It is well known that Cl_2O_2 photolysis plays a dominant role in polar ozone loss.

[18] Both the time evolution of the ozone mixing ratio in Figure 5a and the difference between the SA and PPA versions in Figure 5b show similar variations to those of total ozone. Figure 5c shows an earlier increase of the ClO mixing ratio in the SA version, which corresponds to an earlier increase of the photolysis rate of Cl_2O_2 shown in Figure 5d. The SZA at local noon at 80°S reaches 90° on

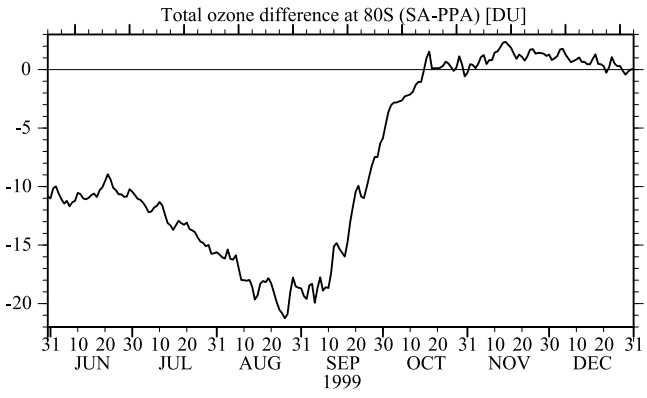

Figure 4. Time evolution of the zonal mean total ozone difference between the SA and PPA versions (SA minus PPA) of the nudging CTM over 80°S from June to December 1999.

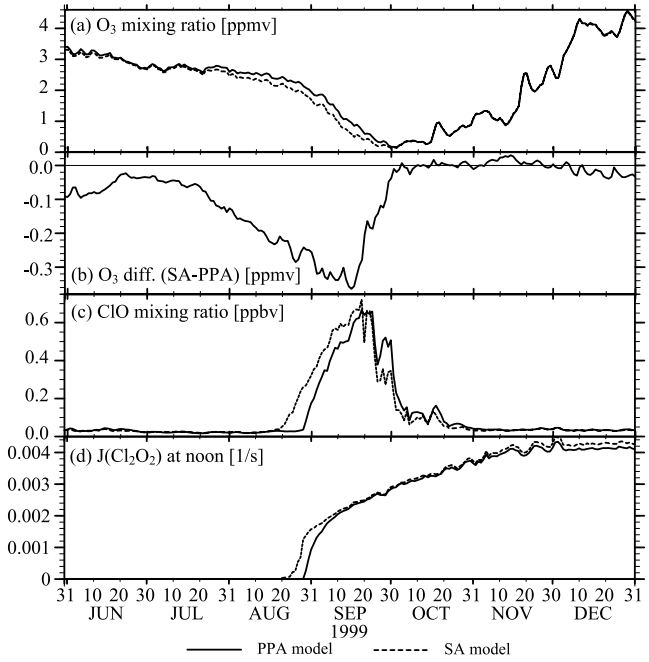

Figure 5. Time evolution of (a) the zonal mean ozone mixing ratio at 80°S and 50 hPa, (b) the difference between the SA and PPA versions (SA minus PPA), (c) the zonal mean ClO mixing ratio, and (d) the photolysis rates of Cl_2O_2 at local noon simulated by the nudging CTM from June to December 1999. Solid and dashed lines in Figures 5a, 5c, and 5d indicate the calculated results from the PPA and SA versions, respectively.

28 August. Therefore the rapid increase of the ClO mixing ratio starts just after 28 August in the PPA version. On the other hand, the ClO mixing ratio in the SA version starts to increase on 18 August by the upward actinic flux at SZAs greater than 90°. As a result, the onset of ozone destruction starts earlier and thus the ozone destruction continues longer in the SA version, which reduces the minimum value of total ozone compared to the PPA version. These results are consistent with the work of *Lary and Pyle* [1991a, 1991b], who suggested the importance of Cl_2O_2 photolysis at SZAs greater than 90° for polar ozone loss.

[19] After the ClO mixing ratio in the PPA version reaches a maximum on the middle of September, the difference in the ozone mixing ratio between the SA and PPA versions diminishes rapidly, as seen in Figure 5a and 5b. During the ozone recovery phase after the end of September, the difference in the ozone amount is very small. This suggests that the ozone variation in the recovery phase is mainly controlled by dynamical processes because the dynamical fields of the nudging CTM are the same in the SA and PPA versions.

[20] Note that the difference both in the total ozone and the ozone mixing ratio between the SA and PPA versions already exists during the polar night, i.e., before the onset of the ozone hole. The reason is discussed in section 5.1.

4.2. Effects of Atmospheric Sphericity on Chemical, Radiative, and Dynamical Coupling Processes of the Polar Stratosphere: Results From the AGCM Ensemble Experiments

4.2.1. Chemistry

[21] Figure 6 shows the ensemble mean difference in the temporal distribution of the zonal mean total ozone between the SA and PPA versions (SA minus PPA). The dark shaded area and light shaded area indicate the 99% and 95% statistical significance levels, respectively, by the t-test. The total ozone around Antarctica in the SA version is lower by 20–40 D.U. than that in the PPA version from September to the following January.

[22] The temporal variations of the zonal mean total ozone at 80°S, the difference between the SA and PPA versions (SA minus PPA), the ozone mixing ratio, and the ClO mixing ratio at 80°S and 50 hPa in the ensemble means from 1 June to the end of February of the following year are shown in Figures 7a–7d. In the ozone loss phase similar results to those from the nudging CTM are obtained. The earlier onset of ozone reduction and the smaller minimum

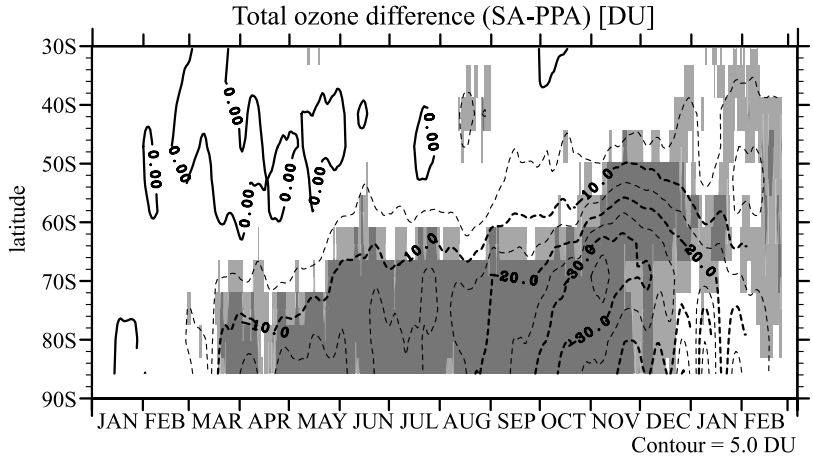

Figure 6. Time-latitude cross section of the zonal mean total ozone difference in the ensemble mean between the SA and PPA versions (SA minus PPA) of the AGCM from January to February of the following year. The dark and light shaded areas show the regions where the differences are statistically significant at the 99% and 95% levels by the t-test, respectively. Smoothed results by 7-day running mean are plotted.

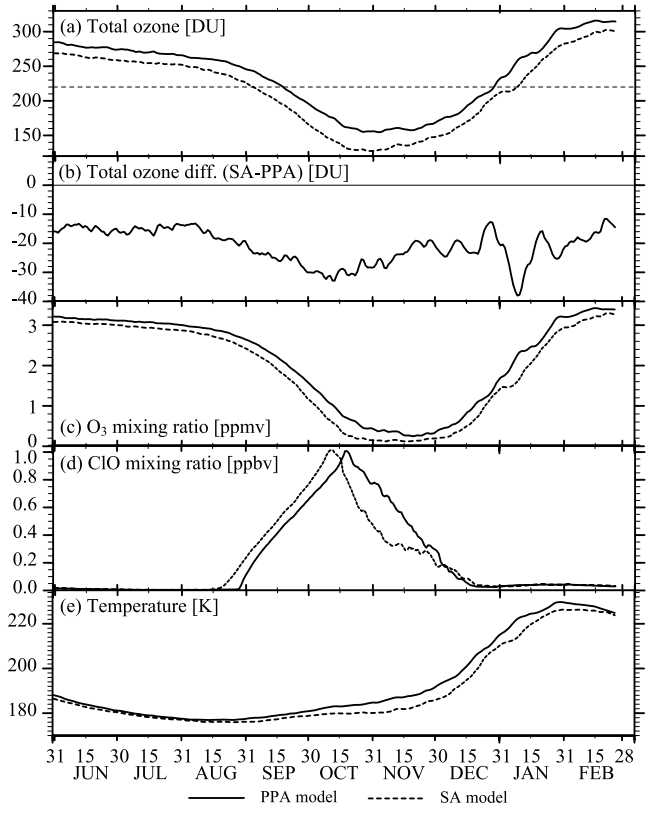

Figure 7. Time evolution of (a) the zonal mean total ozone at 80°S, (b) the difference between the SA and PPA versions (SA minus PPA), (c) the zonal mean ozone mixing ratio at 80°S and 50 hPa, (d) the zonal mean ClO mixing ratio, and (e) the zonal mean temperature in the ensemble mean simulated by the AGCM from June to February of the following year. Solid and dashed lines in Figures 7a and 7c–7e indicate the calculated results from the PPA and SA versions, respectively. The horizontal dashed line in Figure 7a indicates the ozone hole criterion of <220 D.U.

value of the ozone amount in the SA version compared to the PPA version are evident in Figures 7a–7c. Figure 7d indicates that the earlier decrease of ozone in the SA version is caused by the earlier increase of ClO, same as the case of the nudging CTM. In the SA version, the ClO mixing ratio suddenly decreases after the middle of October. Same feature is seen around the South Pole as shown in Figure 8, where the time-latitude cross section of the zonal mean difference of the ensemble mean ClO mixing ratio between the SA and PPA versions (SA-PPA) at 50 hPa is plotted. In this region, O_3 mixing ratio in the SA version of the AGCM becomes almost zero after the middle of October and then Cl starts to react with CH_4.

[23] After the total ozone minimum, the behavior of the ozone variation is different from the results of the nudging CTM. The total ozone in the SA version maintains its values lower than those of the PPA version until the end of the simulation, despite the decrease of the ClO mixing ratio. This behavior during the ozone recovery phase cannot be explained by ozone chemistry alone.

[24] Note that, similar to the nudging CTM, the difference in the ozone value between the SA and PPA versions already exists during the polar night. The reason of this is the same as for the nudging CTM (see section 5.1 for details).

4.2.2. Radiation and Dynamics

[25] In the AGCM with coupled chemistry, polar ozone loss can change the meteorological fields through a change of the radiative energy balance. Actually, the temperatures in the SA version remain cooler than those in the PPA version after the ozone minimum as shown in Figure 7e, where the temporal evolution of the ensemble means of temperature at 80°S and 50 hPa is plotted.

[26] In order to understand this feature, the zonally averaged thermal balance in the lower stratosphere is investigated. The zonally averaged thermal balance is given by

$$\frac{\partial T}{\partial t} = Q_{diabatic} + Q_{dynamical}, \tag{1}$$

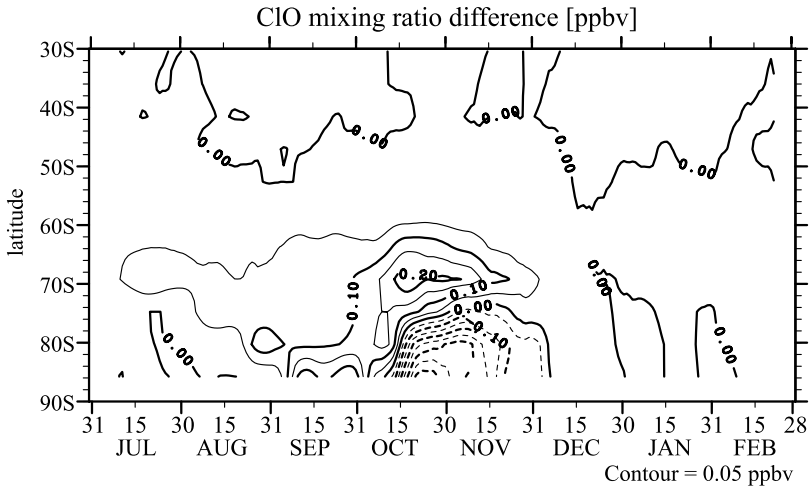

Figure 8. Time-latitude cross section of the zonal mean difference of the ClO mixing ratio in the ensemble mean between the SA and PPA versions (SA minus PPA) of the AGCM at 50 hPa in the Southern Hemisphere from June to February of the following year. Smoothed results by 7-day running mean are plotted.

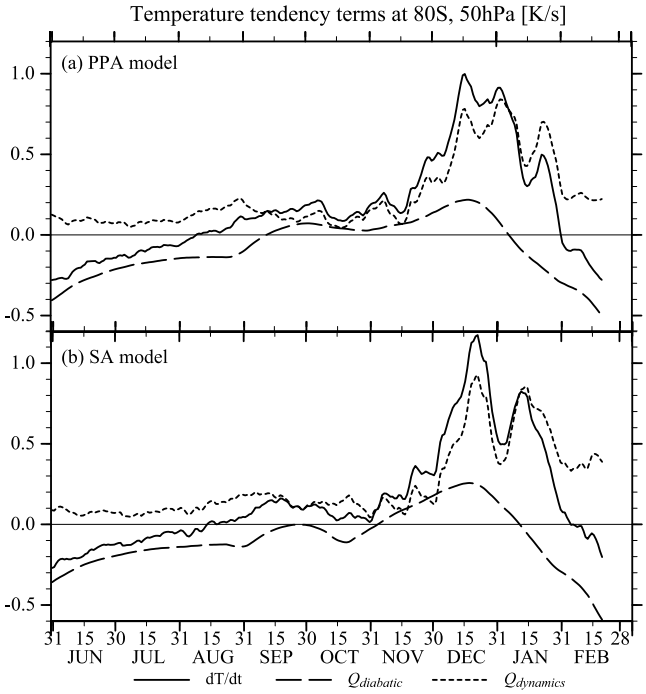

Figure 9. Time evolution of the three terms of the thermal balance equation (equation (1)), zonally averaged at 80°S and 50 hPa in the ensemble mean simulated by (a) the PPA version and (b) the SA version of the AGCM from June to February of the following year. Solid, short-dashed, and long-dashed lines indicate the temperature tendency $(\frac{\partial T}{\partial t})$, the dynamical heating $Q_{dynamical}$, and the diabatic heating $Q_{diabatic}$, respectively. Smoothed results by 10-day running mean are plotted.

where $\frac{\partial T}{\partial t}$ is the temperature tendency, $Q_{diabatic}$ is the net diabatic heating, and $Q_{dynamical}$ is the dynamical heating. The temporal variation of each term of (1) at 80°S and 50 hPa is plotted in Figures 9a and 9b for the PPA and SA versions, respectively. These results are obtained from the ensemble means using a 10-day running mean. The net diabatic heating term in the SA version is smaller than that in the PPA version in September, October, and at the beginning of November, corresponding to the maximum difference of ozone concentration at this time (see Figure 7c). The smaller diabatic heating in the SA version is caused by the decreased shortwave radiation absorption by ozone molecules due to the larger ozone destruction. This leads to a smaller temperature tendency and hence the lower temperature in the SA version. The increase of the dynamical heating term starts after the middle of November in the PPA version, while that in the SA version is delayed about 10 days. These results suggest that some differences in the dynamical fields between the SA and PPA versions occur owing to the different extent of the ozone depletion.

[27] Figure 10 shows the difference of the zonal mean zonal wind in the ensemble mean between the SA and PPA versions (SA minus PPA) over 64°S, where a zonal wind maximum exists. The zonal mean zonal wind of the upper stratosphere in the SA version is larger than that in the PPA version from the middle of October to the end of January of the following year. This indicates that the onset of the westerly wind deceleration is delayed and therefore the duration of the polar vortex is longer in the SA version.

[28] The stronger polar vortex in the SA version is caused by the larger latitudinal gradient of temperature, resulted from the smaller net diabatic heating due to the larger polar ozone depletion in the SA version. A resultant delay of the polar vortex breakup prevents the transport of ozone-rich air masses at lower latitudes into the polar region. This is a possible reason that the ozone recovery over Antarctica is delayed in the SA version.

4.2.3. Variances of the Ensemble Experiments in the Ozone Recovery Phase

[29] In sections 4.2.1 and 4.2.2, only the results of the ensemble means are described. However, after the middle of December, large ozone variances are shown over Antarctica (see Figure 6), when the ozone recovery is dynamically controlled. In this section, all ensemble members are examined to investigate whether each member actually shows the

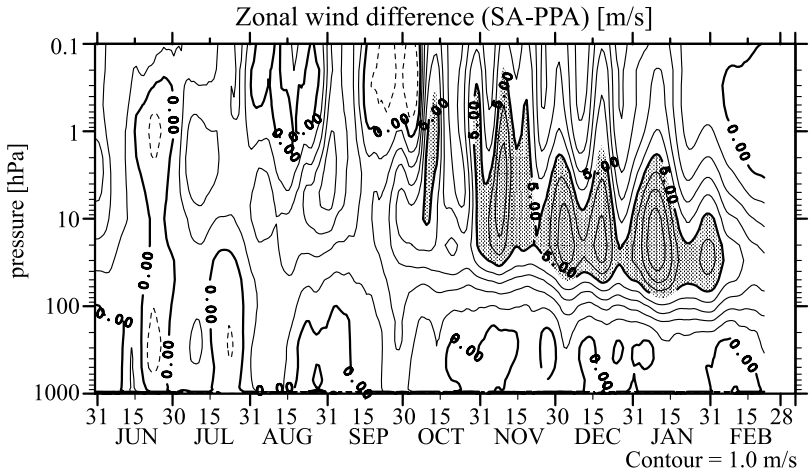

Figure 10. Time-height cross section of the zonal mean zonal wind difference in the ensemble mean between the SA and PPA versions (SA minus PPA) of the AGCM over 64°S from June to February of the following year. The shaded areas represent the difference values over 5 m s^{-1}. Smoothed results by 7-day running mean are plotted.

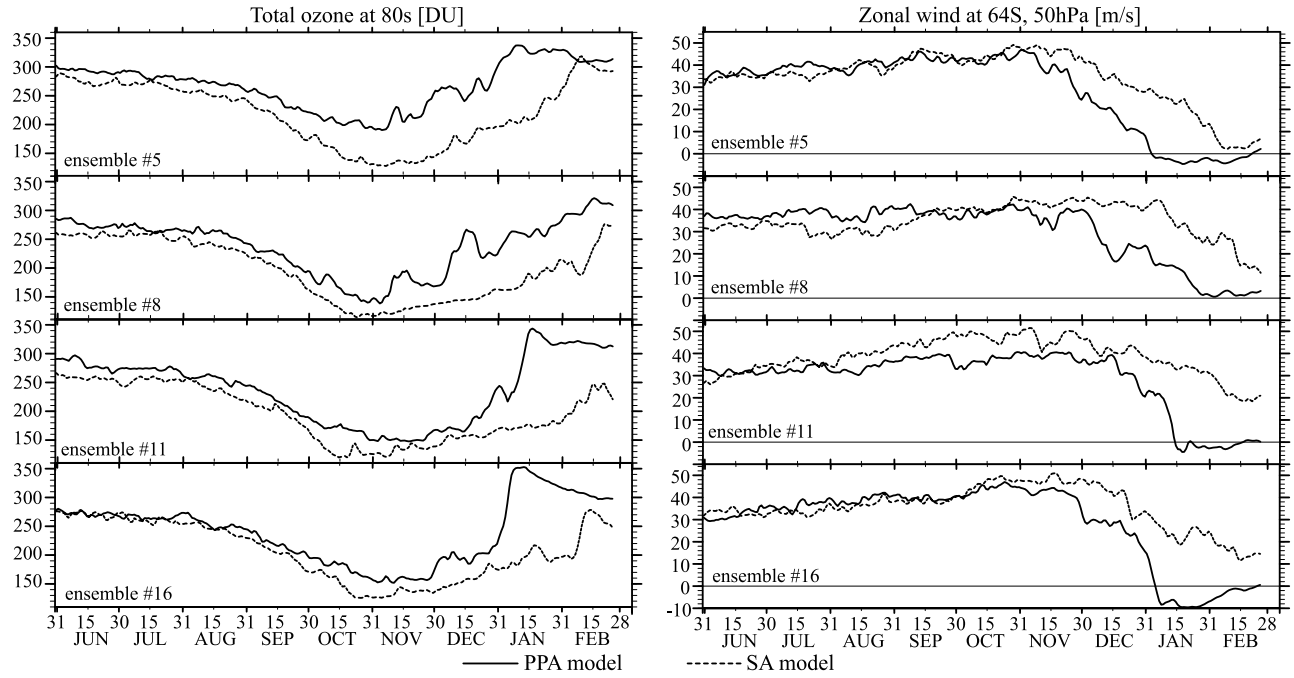

Figure 11. Time evolution of the zonal mean total ozone at 80°S and zonal mean zonal wind at 64°S and 50 hPa of typical ensemble members 5, 8, 11, and 16 in the PPA version (solid line) and in the SA version (dashed line) of the AGCM.

variances that are expected from the statistical theory in the ozone recovery period.

[30] In all members, there are strong correlations between the zonal mean total ozone increase and the zonal mean zonal wind deceleration during the ozone recovery phase. This indicates that dynamical processes certainly play an important role in the ozone recovery period. Most ensemble members show that the polar vortex breakup and ozone recovery processes are delayed in the SA version of the model, which is expected from the effects of atmospheric sphericity on the chemical, radiative, and dynamical processes in the stratosphere, as described in previous section. Figure 11 shows the typical time evolution of the zonal mean total ozone at 80°S and the zonal mean zonal wind at 64°S and 50 hPa in the SA and PPA versions (for ensemble members 5, 8, 11, and 16). However, four unusual cases

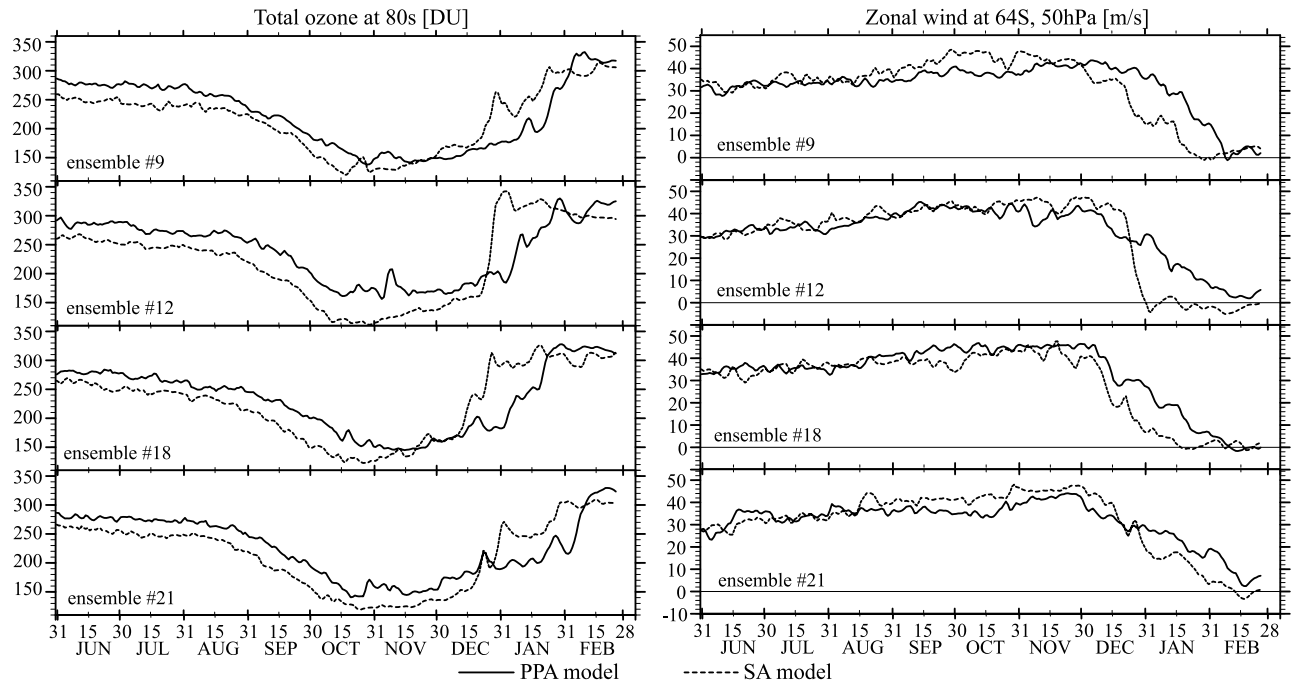

Figure 12. Same as Figure 11 but for the unusual ensemble members 9, 12, 18, and 21.

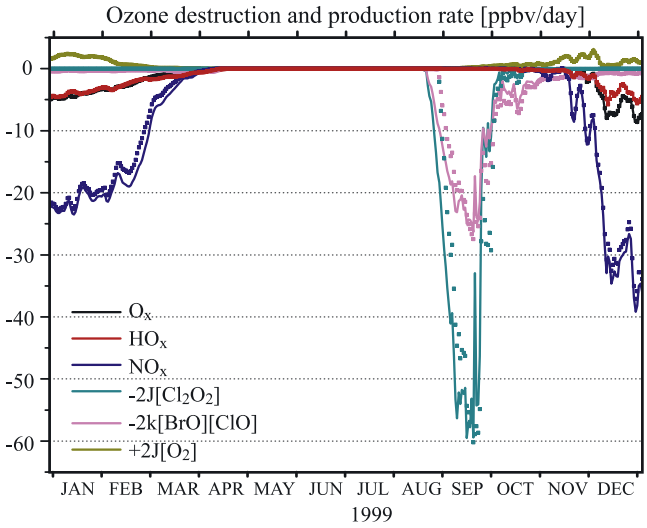

Figure 13. Time evolution of the zonal mean ozone destruction and production terms at 80°S and 50 hPa in the SA version (solid lines) and the PPA version (symbols) of the nudging CTM from January to December 1999. Black, red, dark blue, dark green, pink, and dark yellow colors indicate the ozone destruction rates due to O_x, HO_x, NO_x, the ClO-ClO cycle, the BrO-ClO cycle, and the ozone production rate due to oxygen photolysis, respectively.

(ensemble members 9, 12, 18, and 21) are found, where the total ozone recovery and the polar vortex breakup occur earlier in the SA version, as seen in Figure 12.

[31] If these unusual cases are ignored, the total ozone difference in the ensemble means between the SA and PPA versions becomes statistically significant at the 95% level until the middle of January of the following year (not shown). Therefore the large variance in the ozone recovery period is caused by the unusual behavior of a few ensemble members, which most members do not show. These results justify the hypothesis from the ensemble means that the chemical, radiative, and dynamical coupling processes in the stratosphere, described in previous section, mainly explain the delays of the polar vortex breakup and the resultant ozone recovery over Antarctica in the SA version of the AGCM. Further analysis of the unusual cases is described in section 5.2.

5. Discussion

5.1. Analysis of the Different Time Evolutions of Polar Ozone Between the SA and PPA Model Versions Before the End of the Polar Night

[32] In sections 4.1 and 4.2 we indicated that the differences in the total ozone at 80°S and the ozone mixing ratio at 80°S and 50 hPa between the SA and PPA versions already existed even before the end of the polar night. In the nudging CTM these differences started to increase from mid-February to mid-April and then remained almost constant until the end of June. After that, at the beginning of July, the difference started to increase again and reached a maximum at the end of August. The situation was almost the same in the AGCM.

[33] In order to investigate the initial increase of the difference, time evolution of the zonal mean ozone destruction and production terms at 80°S and 50 hPa in the SA and PPA versions of the nudging CTM is plotted in Figure 13. The ozone destruction rates due to O_x, HO_x, and NO_x processes are calculated following the method of *Fahey et al.* [2000]. The "$-2J[Cl_2O_2]$" and "$-2k[ClO][BrO]$" represent the ozone destruction terms of the ClO-ClO and ClO-BrO cycles, respectively, and the "$2J[O_2]$" represents the ozone production term. From mid-February to the onset of the polar night (mid-April), the NO_x, HO_x, and O_x cycles are the main contributors to the ozone destruction, and the contribution of the ClO_x and BrO_x cycles are negligible. In the SA version, the ozone destruction terms of the NO_x, HO_x and O_x cycles are slightly larger and continue a little longer than those in the PPA version before the onset of polar night. This is due to the actinic flux at SZAs larger than 90° and is the reason for the initial increase of the difference.

[34] For the investigation of the latter increase of the difference, which starts at the beginning of July, a passive tracer ozone experiment using the SA version of the nudging CTM is executed. In the experiment, the chemical change of ozone is ignored at and to the south of 80°S and at 50 hPa from 20 June, slightly before the latter increase of the difference starts. Figure 14 shows the temporal evolution of the ozone mixing ratio in the original experiment and the passive tracer ozone experiment. The difference between the solid and dotted lines in Figure 14 represents the effect of local chemical ozone destruction at and to the south of 80°S and at 50 hPa. Just after 18 August, the difference begins to increase because the upward actinic flux initiated the local photochemical ozone loss (see section 4.1). Before the end of the polar night, on the other hand, there are almost no differences between the experiments and the passive tracer ozone experiment already shows the larger decline in ozone concentration compared to the PPA version. All these results indicate that the time evolution of ozone at 80°S and 50 hPa is affected by the advection of low-ozone concentration air masses from lower latitudes

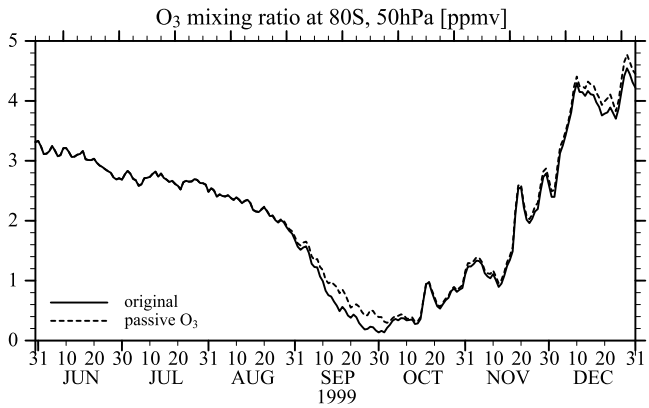

Figure 14. Time evolution of the zonal mean ozone mixing ratio at 80°S and 50 hPa from June to December 1999 in the original experiment and the passive tracer ozone experiment using the SA version of the nudging CTM. Solid and dashed lines indicate the results from the original experiment and the passive tracer ozone experiment, respectively. Ozone is assumed to be a passive tracer at and to the south of 80°S and at 50 hPa from 20 June.

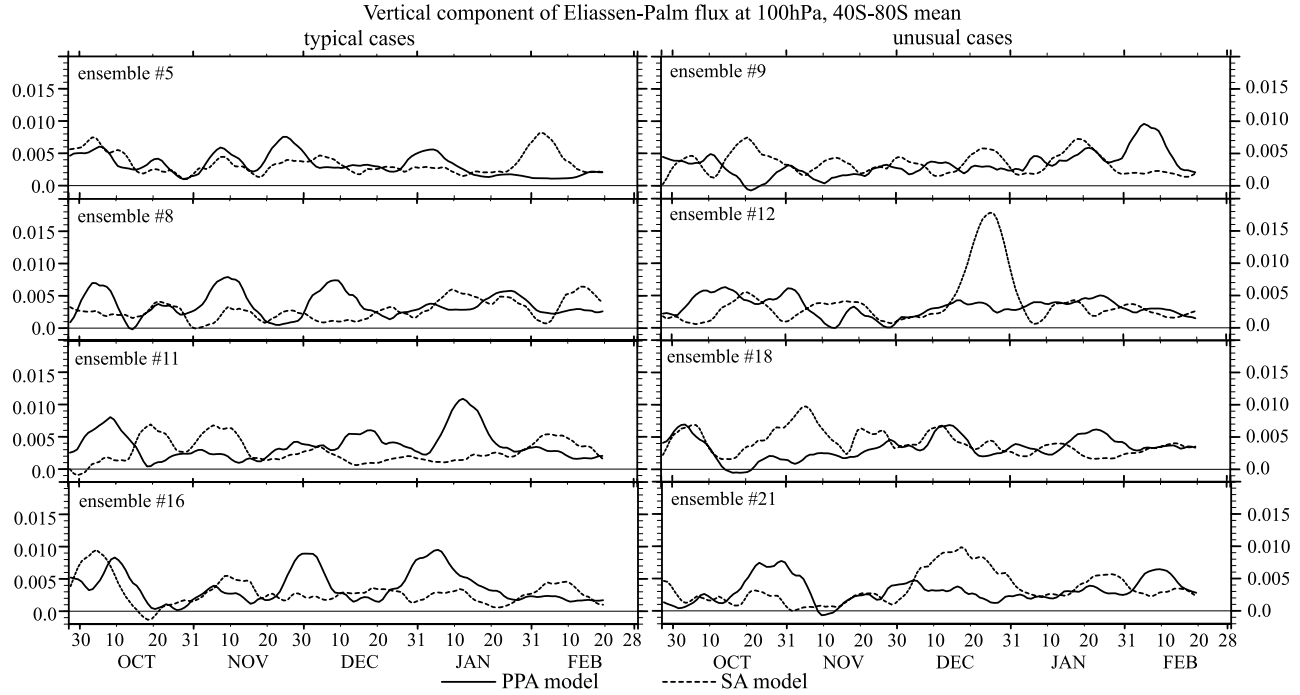

Figure 15. Time evolution of the vertical component of the EP flux averaged over 40°–80°S and at 100 hPa in the PPA version (solid line) and the SA version (dashed line) of the AGCM. (left) Typical cases (5, 8, 11, and 16) and (right) unusual cases (9, 12, 18, and 21).

and higher altitude, where ozone destruction processes start earlier because of the actinic flux at SZAs greater than 90°.

5.2. Analysis of the Statistical Variances of the Ensemble Experiments in the Ozone Recovery Phase

[35] The Eliassen-Parm (EP) flux for the eight ensemble members in Figures 11 and 12 is calculated in order to investigate what causes the behavior of the zonal mean total ozone and the zonal mean zonal wind in the unusual cases. Figure 15 shows the time evolution of the vertical component of the EP flux averaged over 40°–80°S and 100 hPa for the eight ensemble members. In the unusual cases shown in the right column of Figure 15, the magnitude of the EP flux in the SA version becomes larger than that in the PPA version just before the total ozone in the SA version rapidly rises (see also Figure 12 around 20 October in 9, around 25 December in 12, around 5 November in 18, and around 15 December in 21). The EP flux at this level expresses the wave flux from the troposphere into the stratosphere. Therefore, in the SA version of the unusual members, the wave flux from the troposphere into the stratosphere dominantly controls the timing of the ozone recovery, overwhelming the effects of the atmospheric sphericity on the modeled radiation field in the Antarctic stratosphere. In the typical cases, on the other hand, the correlation between the EP flux enhancement and the ozone rise in the SA version is not as clear as that in the unusual cases. For example, the EP flux enhancement in the SA version is found around 20 October and 10 November in 11 and around 5 October in 16, but the total ozone amount in the SA version did not exceed that in the PPA version just after these dates (see Figure 11). The EP flux at 200 hPa is also examined and a very similar result is found (not shown).

[36] In most cases, the polar vortex breakup is delayed in the SA version because of the chemical-radiative-dynamical coupling effects of the atmospheric sphericity in the stratosphere. However, the analysis of each ensemble member shows that the increased wave flux from the troposphere is sometimes a more effective determinant of the timing of the polar vortex breakup than the effects of atmospheric sphericity in the stratosphere.

5.3. Influence of Neglecting Refraction and Heating Due to the Solar Radiation Flux at SZAs Larger Than 90°

[37] The new radiative transfer scheme does not include the two factors, namely, refraction and the heating effects of the radiation flux at SZAs larger than 90°. Neglecting these processes may have an influence on Antarctica during the ozone hole period [*Lary and Balluch*, 1993; *Balluch and Lary*, 1995; *Herman et al.*, 1995; *Swartz et al.*, 1999; *Trentmann et al.*, 2003; *Uhl and Reddmann*, 2004].

[38] By considering the effects of refraction, maximum SZA at the edge of the polar twilight region becomes larger by about 1° at 50 hPa (i.e., the apparent SZA is 1° less), which would make the onset of the ozone loss occur several days earlier. Furthermore, the refraction effects increase the optical transmittance and may strengthen the ozone destruction due to photochemical catalysis [*Uhl and Reddmann*, 2004]. Thus the introduction of refraction will enhance the effects of atmospheric sphericity.

[39] With respect to heating rates, *Lary and Balluch* [1993] suggested that ignoring the heating effects at SZAs larger than 90° might lead to the large latitudinal heating rate gradient and misrepresent the structure of the general circulation, particularly in the region close to the polar night (and polar day). Furthermore, it may be possible that the

increased temperature in the polar stratosphere by the heating due to the solar radiation flux at SZAs larger than 90° prevents heterogeneous chemistry and attenuates further ozone loss. However, the radiative heating at SZAs larger than 90° may have a dominant effect only in the period before the radiation flux at SZAs smaller than 90° reaches. Therefore the effect on the timing of polar vortex breakup might be limited. These possibilities must be examined carefully in a future study.

6. Conclusions

[40] The effects of atmospheric sphericity are incorporated into the CCSR/NIES nudging CTM and AGCM with coupled chemistry. The plane-parallel radiative transfer scheme of both models is modified using a pseudospherical approximation. We perform the integration of the nudging CTM and the ensemble runs of the AGCM with coupled chemistry for both the SA and PPA versions. The chemical processes and coupling effects of the chemical, radiative, and dynamical processes over Antarctica during an ozone hole period are analyzed.

[41] In the SA versions of both the nudging CTM and the AGCM, the onset of an ozone loss over Antarctica shifts to earlier dates, and the minimum value of the total ozone becomes lower in comparison with the corresponding PPA versions. The earlier reduction in the ozone mixing ratio in the SA version is caused by an earlier increase of the ClO mixing ratio, which is initiated by the upward actinic flux at SZAs greater than 90°. During the ozone recovery period, however, the ozone distribution becomes almost the same in the SA and PPA versions of the nudging CTM, while in the AGCM the ozone amount of the SA version remains at lower values compared to that of the PPA version.

[42] In the SA version of the AGCM, the larger ozone loss over Antarctica makes the diabatic heating smaller and temperatures lower in comparison with the PPA version. This enhances the latitudinal gradient of temperature and thus strengthens the polar vortex in the SA version. These processes cause the delayed ozone recovery over Antarctica by preventing the transport of ozone-rich air masses from lower latitudes into the polar region.

[43] In the AGCM ensemble experiment, there are large ozone variances after the middle of December, when the ozone recovery is controlled dynamically. Most ensemble members show the delay of the polar vortex breakup in the SA version, but a few members show opposite results. In the latter members, the polar vortex breakup in the SA version is strongly affected by the enhanced wave flux from the troposphere, which causes the variances in the ozone recovery period. Most members, however, do not show large statistical variances, that justifies the conclusions from the ensemble means.

[44] **Acknowledgments.** The authors thank the late A. Numaguti and other members for the development of the CCSR/NIES AGCM, T. Imamura for useful discussions, and anonymous reviewers for helpful comments. Computations were made on a NEC SX-6 computer at CGER (Center for Global Environmental Research) of the NIES. The GFD-DENNOU library and GTOOL were used for drawing the figures. This work was supported by the Global Environmental Research Fund of the Ministry of the Environment (MOE) of Japan and by a grant-in-aid for scientific research from the Ministry of Education, Culture, Sports, Science and Technology (MEXT) of Japan (16540405).

References

Akiyoshi, H. (1997), Development of a global 1-D chemically radiatively coupled model and an introduction to the development of a chemically coupled General Circulation Model, *CGER's Supercomput. Monogr. Rep.*, *4*, 69 pp., Natl. Inst. For Environ. Stud., Tsukuba, Japan.

Akiyoshi, H., S. Sugata, T. Sugita, H. Nakajima, H. Hayashi, J. Kurokawa, and M. Takahashi (2002a), Low-N_2O air masses after the breakdown of the Arctic polar vortex in 1997 simulated by the CCSR/NIES nudging CTM, *J. Meteorol. Soc. Jpn.*, *80*, 451–463.

Akiyoshi, H., S. Sugata, T. Sugita, H. Nakajima, H. Hayashi, J. Kurokawa, and M. Takahashi (2002b), Correction to "Low-N_2O air masses after the breakdown of the Arctic polar vortex in 1997 simulated by the CCSR/NIES nudging CTM," *J. Meteorol. Soc. Jpn.*, *80*, 1308.

Akiyoshi, H., T. Sugita, H. Kanzawa, and N. Kawamoto (2004), Ozone perturbations in the Arctic summer lower stratosphere as a reflection of NO_x chemistry and planetary scale wave activity, *J. Geophys. Res.*, *109*, D03304, doi:10.1029/2003JD003632.

Allen, M., and J. Frederick (1982), Effective photodissociation cross section for molecular oxygen and nitric oxide in the Schumann-Runge bands, *J. Atmos. Sci.*, *39*, 2066–2075.

Balluch, M., and D. J. Lary (1995), Reply, *Bull. Am. Meteorol. Soc.*, *52*, 383–387.

Chipperfield, M. P., T. Glassup, I. Pundt, and O. V. Rattigan (1998), Model calculation of stratospheric OBrO indicating very small abundances, *Geophys. Res. Lett.*, *25*, 3575–3578.

Dahlback, A., and K. Stamnes (1991), A new spherical model for computing the radiation field available for photolysis and heating at twilight, *Planet. Space Sci.*, *39*, 671–683.

Dvortsov, V. L., S. G. Zvenigorodsky, and S. P. Smyslaev (1992), On the use of Isaksen-Luther method of computing photodissociation rates in photochemical models, *J. Geophys. Res.*, *97*, 7593–7601.

Fahey, D. W., et al. (2000), Ozone destruction and production rates between spring and autumn in the Arctic stratosphere, *Geophys. Res. Lett.*, *27*, 2605–2608.

Herman, B. M., T. Caudill, D. Flittner, and K. N. Liou (1995), Comments on "Solar heating rates: The importance of spherical geometry," *Bull. Am. Meteorol. Soc.*, *52*, 380–382.

Kylling, A., T. Danielsen, M. Blumthaler, J. Schreder, and B. Johnsen (2003), Twilight tropospheric and stratospheric photodissociation rates derived from balloon borne radiation measurements, *Atmos. Chem. Phys.*, *3*, 377–385.

Lamago, D., M. Dameris, C. Schnadt, V. Eyring, and C. Brühl (2003), Impact of large solar zenith angles on lower stratospheric dynamical and chemical processes in a coupled chemistry-climate model, *Atmos. Chem. Phys.*, *3*, 1981–1990.

Landgraf, J., and P. J. Crutzen (1998), An efficient method for online calculations of photolysis and heating rates, *J. Atmos. Sci.*, *55*, 863–878.

Lary, D. J., and M. Balluch (1993), Solar heating rates: The importance of spherical geometry, *Bull. Am. Meteorol. Soc.*, *50*, 3983–3993.

Lary, D. J., and J. A. Pyle (1991a), Diffuse radiation, twilight, and photochemistry—I, *J. Atmos. Chem.*, *13*, 373–392.

Lary, D. J., and J. A. Pyle (1991b), Diffuse radiation, twilight, and photochemistry—II, *J. Atmos. Chem.*, *13*, 393–406.

Lary, D. J., J. A. Pyle, C. R. Webster, and R. D. May (1991), The bliss measurements of NO_2: Some new insights, *Geophys. Res. Lett.*, *18*, 2261–2263.

Levy, H., II (1974), Photochemistry of the troposphere, *Adv. Photochem.*, *9*, 369–524.

Minschwaner, K., R. J. Salawitch, and M. B. McElroy (1993), Absorption of solar radiation by O_2: Implications for O_2 and lifetimes of N_2O, $CFCl_3$, and CF_2Cl_2, *J. Geophys. Res.*, *98*, 10,543–10,561.

Müller, R., T. Peter, P. J. Crutzen, H. Oelhaf, G. P. Adrian, T. von Clarmann, A. Wegner, U. Schmidt, and D. Lary (1994), Chlorine chemistry and the potential for ozone depletion in the Arctic stratosphere in the winter of 1991/92, *Geophys. Res. Lett.*, *21*, 1427–1430.

Nagashima, T., M. Takahashi, M. Takigawa, and H. Akiyoshi (2002), Future development of the ozone layer calculated by a general circulation model with fully interactive chemistry, *Geophys. Res. Lett.*, *29*(8), 1162, doi:10.1029/2001GL014026.

Nakajima, T., and M. Tanaka (1986), Matrix formulation for the transfer of solar radiation in a plane-parallel scattering atmosphere, *J. Quant. Spectrosc. Radiat. Transfer*, *35*, 13–21.

Nakajima, T., M. Tsukamoto, Y. Tsuhima, A. Numaguti, and T. Kimura (2000), Modeling of the radiative process in an atmospheric general circulation model, *Appl. Opt.*, *39*, 4869–4878.

Numaguti, A. (1993), Dynamics and energy balance of the Hadley circulation and the tropical precipitation zones: Significance of the distribution of evaporation, *J. Atmos. Sci.*, *50*, 1874–1887.

Numaguti, A., M. Takahashi, T. Nakajima, and A. Sumi (1995), Development of an atmospheric general circulation model, in *Climate System*

Dynamics and Modeling, *Reports of A New Program for Creative Basic Research Studies: Studies of Global Environmental Change With Special Reference to Asia and Pacific Region*, vol. I-3, pp. 1–27, edited by T. Matsuno, Cent. for Clim. Syst. Res., Univ. of Tokyo, Tokyo.

Numaguti, A., S. Sugata, M. Takahashi, T. Nakajima, and A. Sumi (1997), Study on the climate system and mass transport by a climate model, in *CGER's Supercomput. Monogr. Rep.*, *CGER-I025-'97,* vol. 3, 91 pp., Natl. Inst. for Environ. Stud., Tsukuba, Japan.

Perner, D., T. Klüpfel, U. Parchatk, A. Roth, and T. Jørgensen (1991), Ground-based UV-VIS spectroscopy: Diurnal OClO-profiles during January 1990 above Søndre Strømfjord, Greenland, *Geophys. Res. Lett.*, *18*, 787–790.

Rattigan, O. V., D. J. Lary, R. L. Jones, and R. A. Cox (1996), UV-visible absorption cross section of gaseous Br_2O and HOBr, *J. Geophys. Res.*, *101*, 23,021–23,033.

Rees, D., J. J. Barnett, and K. Labitzke (Eds.) (1990), *COSPAR International Reference Atmosphere: 1986, Part II, Middle Atmosphere Models*, *Adv. Space Res.*, *10*, 519 pp.

Röth, E.-P. (1992), A fast algorithm to calculate the photon flux in optically dense media for use in photochemical models, *Ber. Bunsenges Phys. Chem.*, *96*, 417–420.

Röth, E.-P. (2002), Description of the anisotropic radiation transfer model ART to determine photodissociation coefficients, report, Inst. fur Stratospharische Chem., Forsch. Julich, Julich, Germany.

Swartz, W. H., S. A. Lloyd, T. L. Kusterer, D. E. Anderson, C. T. McElroy, and C. Midwinter (1999), A sensitivity study of photolysis rate coefficients during POLARIS, *J. Geophys. Res.*, *104*, 26,725–26,735.

Takigawa, M., M. Takahashi, and H. Akiyoshi (1999), Simulation of ozone and other chemical species using a Center for Climate System Research/National Institute for Environmental Studies atmospheric GCM with coupled stratospheric chemistry, *J. Geophys. Res.*, *104*, 14,003–14,018.

Trentmann, J., H. Bovensmann, V. Eyring, R. W. Müller, and J. P. Burrows (2003), Impact of accurate photolysis calculations on the simulation of stratospheric chemistry, *J. Atmos. Chem.*, *44*, 225–240.

Uhl, R., and T. Reddmann (2004), Divergence of sun-rays by atmospheric refraction at large solar zenith angles, *Atmos. Chem. Phys.*, *4*, 1399–1405.

World Meteorological Organization (1999), Scientific assessment of ozone depletion: 1998, *Global Ozone Res. and Monit. Proj. Rep. 44*, Geneva, Switzerland.

H. Akiyoshi, T. Nagashima, and H. Nakane, National Institute for Environmental Studies, 16-2 Onogawa, Tsukuba 305-8506, Japan. (hakiyosi@nies.go.jp; nakane@nies.go.jp; nagashima.tatsuya@nies.go.jp)

J. Kurokawa, Fujitsu FIP Corporation, TIME24 BLDG., 2-45 Aomi, Koto-Ku, Tokyo 135-8686, Japan. (kurokawa@fip.fujitsu.com)

H. Masunaga, Department of Atmospheric Science, Colorado State University, Fort Collins, CO 80523, USA. (masunaga@atmos.colostate.edu)

T. Nakajima and M. Takahashi, Center for Climate System Research, University of Tokyo, 5-1-5 Kashiwanoha, Kashiwa, Chiba 277-8568, Japan. (teruyuki@ccsr.u-tokyo.ac.jp; masaaki@ccsr.u-tokyo.ac.jp)